New descriptors of connectivity-bottleneck effects improve understanding and prediction of diffusive transport in pore geometries

(article starts on next page)

Contents lists available at ScienceDirect

Computational Materials Science

Full length article

New descriptors of connectivity-bottleneck effects improve understanding and prediction of diffusive transport in pore geometries

Sandra Barman [a],*, Holger Rootzén [b], David Bolin [c]

[a] *Product Design, RISE Research Institutes of Sweden, Gothenburg, Sweden*
[b] *Department of Mathematical Sciences, Chalmers University of Technology and the University of Gothenburg, Gothenburg, Sweden*
[c] *CEMSE Division, King Abdullah University of Science and Technology, Thuwal, Saudi Arabia*

ARTICLE INFO

ABSTRACT

Bottlenecks can drastically reduce transport through porous materials. Previous work has concentrated on constriction-bottlenecks caused by variations in pore size. Here we study connectivity-bottlenecks, which are caused by many paths in the pore network passing through the same small part of the material. We develop three new connectivity descriptors, geodesic channel-strength, pore size-channels, and the closed pore-tortuosity that capture these effects.

Five sets of computer-generated pore geometries with a wide variation in characteristics were used to evaluate the effect bottlenecks have on diffusive transport. We show that low connectivity as measured by the new bottleneck descriptors, can decrease diffusive transport drastically, but that in these data sets constriction-bottlenecks had a smaller effect. We also show that path-lengths and connectivity-bottlenecks can be highly correlated and adjustments using theoretical models of diffusive transport can help separate the effects. We provide a freely available software MIST that can be used to measure connectivity-bottleneck effects.

1. Introduction

With advances in microscopy technology, porous materials can now be imaged in great detail [1–3]. To make use of the images it is important to be able to quantify properties of the pore structure. The quantification can then be used to compare different materials, and to explain material properties such as diffusive transport rate, thermal conductivity, electrical conductivity and fluid permeability in terms of the pore geometry. A next step is to use this knowledge to optimize the design of the material. This type of material quantification and optimization has applications in biomedical and pharmaceutical science [4–6], composite materials design [7], electrochemical engineering [8], and several other areas. However, often only basic pore geometry descriptors such as pore size, surface area and porosity are used to predict conductivity processes [9].[1] Such geometry descriptors cannot capture bottleneck and other complex effects that the connectivity of the pore network has on the material's properties. We need more sophisticated methods for this.

Bottleneck effects are thought to be important for determining diffusive transport and related processes [11–14]. Previous work show that quantification of bottlenecks can be useful for correlating the pore geometry with these processes, both for diffusive transport, electrical conductivity and fluid permeability, see e.g. [9,14–17]. The work in these papers have all been based on the idea of constriction-bottleneck effects, where the type of bottlenecks considered are caused by varying pore sizes across the pore network. The constrictivity descriptor introduced in [14] has been shown to be effective at capturing this type of bottleneck.

However, in a poorly connected porous material, bottlenecks effects can also occur when many paths through the pore network converge in a small portion of the material. We term this a connectivity-bottleneck. Connectivity-bottleneck effects are often observed in materials with large-scale inhomogeneities, such as the poorly connected polymer films studied in [18,19].

The two types of bottlenecks, connectivity-bottlenecks and constrictivity-bottlenecks, are illustrated in Fig. 1. The effect on diffusive flux is similar for both types of bottlenecks. Higher flux within each bottleneck, encircled in red, is contrasted against relatively low flux in the structure leading into and out of the bottleneck.

Connectivity-bottleneck effects cause an inhomogeneous profile of diffusion, permeability or conductivity, with high transport (conductivity) through well-connected regions and low transport (conductivity)

---

* Corresponding author.
  E-mail address: sandra.barman@ri.se (S. Barman).
  [1] Note that tortuosity factor, computed in e.g. TauFactor [10] and presented in [9], is not a geometry descriptor but is derived from transport or conductivity measurements, see the discussion in Section 2.
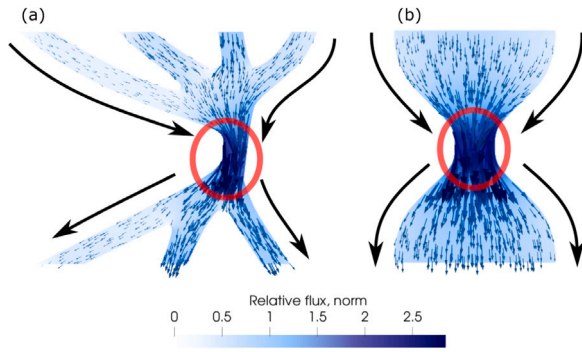
Fig. 1. Illustration of the two types of bottlenecks in simple pore structures. (a) A connectivity-bottleneck and (b) a constriction-bottleneck. Diffusive flux computed in these simple structures are shown, with bottlenecks circled in red. The flux direction is indicated by arrows within the structures. Larger arrows correspond to higher flux.

through poorly connected regions. This reduces the efficiency of the transport (conductivity) and can cause high stress on well-connected regions. In the case of electrical conductivity through porous battery electrodes, e.g., this type of inhomogeneous conductivity profile can cause early degradation and safety issues [20,21]. In the examples seen in Fig. 1, this is illustrated by the high flux within the bottlenecks and low flux in other parts of the structure. The efficiency of the transport is around 50% that of an optimal structure for the connectivity bottleneck (Fig. 1(a)), and around 70% of that of an optimal structure for the constriction bottleneck (Fig. 1(b)). Here the efficiency is measured by the transport ratio defined below.

Although we focus on diffusive transport, the same equations govern electrical conductivity and so the results apply equally to both. In applications such as pharmaceutical science, packaging and hygiene products, diffusive transport can be the main phenomena of interest. In applications such as electrochemical devices, complex phenomena govern the behaviour of the structure with interactions between e.g. ion transport, electrochemical reactions and electrical conductivity. Results presented in this paper, where the effect of bottlenecks caused by e.g. large scale inhomogeneities, are just as important for all of these applications. For the first category of applications where diffusive transport is the main interest, see [18]. Work such as [20–23] show that understanding the impact of complex pore network geometries are essential also for electrochemical devices, which makes quantifying and capturing the effect of bottlenecks important also for such application.

When constructing new methods for capturing connectivity bottleneck effects, we look to established methodology already used for quantifying other aspects of the connectivity of pore networks. Geodesic tortuosity and related geometric tortuosity descriptors have previously been shown to be highly efficient at predicting diffusive transport, permeability and equivalent processes [14,17,24]. In this paper we introduce three additional descriptors which are based on geodesic paths/geodesic tortuosity and which capture different aspects of connectivity-bottlenecks: our recently introduced geodesic channel-strength descriptor [18] and two new ones, the pore size-channel descriptor and the closed-pore-tortuosity descriptor.

The geodesic channel-strength descriptor is based on pores with many geodesic paths passing through it. However such a pore may not be a severe bottleneck if its size is large, or if there are alternative pathways that can relieve the pressure on that pore. The pore size-channel descriptor is similar to the geodesic channel-strength but additionally takes pore sizes into account. The closed-pore-tortuosity descriptor captures how much longer paths through the pore structure become if a pore with a high channel-strength is closed. The introduction of these descriptors give useful new understanding of pore structures, we believe. Examples of this are given by the small illustrative set of pore structures shown in Fig. 2, Fig. 3 and in Table 3. These examples show

how the bottleneck effects illustrated in Fig. 1 apply to more complex pore structures, and how the new method geodesic channel-strength can be used to quantify connectivity-bottleneck effects.

To evaluate the impact connectivity-bottlenecks have on diffusive transport and the predictive power of our new descriptors, we generated four large sets of pore structures with a wide range of path length and bottleneck effects. The first of these, the polymer film data set came from a model developed to simulate the pore structures in coatings of medical pellets. Two other, the Bottlenecks 1 and 2 data sets, were obtained from simpler network models, also inspired by polymer film pore structures. A fourth dataset, the reference data set, was constructed with pore structures which have varying path lengths but no bottleneck effects. Diffusion through the pore structures was computed with the software Gesualdo [25].

We fitted physically motivated logarithmic multiplicative regression models, below called core models, with rescaled computed diffusive transport rate as response variable and compared our three new connectivity-descriptors to the existing descriptors constrictivity, pore size and geodesic tortuosity by computing their predictive power. The main result obtained from the regression analysis was that for our data sets the geodesic tortuosity has the strongest predictive power, and that adding the connectivity descriptors to the prediction equation improves accuracy more than the existing pore geometry descriptors constrictivity and pore size. Connectivity-bottlenecks and path-lengths were also found to be highly correlated, so separating them through the geodesic tortuosity and the connectivity-bottleneck descriptors presented in this paper can be challenging when not using physically motivated models.

The next section provides some background on diffusion in porous materials. Section 3 gives an overview of existing descriptors used for pore geometry quantification and introduces our new connectivity descriptors and Section 4 describes the numerical experiment and the computation methods. Section 5 presents the results of the numerical simulations and the regression modelling, and the following sections contain a discussion of the results and our final conclusions. We throughout indicate how the freely available software [26] can be used for interactive exploration of pore structures, and in particular of connectivity-bottleneck effects.

2. Diffusive transport through pore structures

Diffusion is governed by the equation $\mathbf{J} = -D_0 \nabla c$ in combination with mass conservation $\frac{\partial c}{\partial t} = \nabla \cdot \mathbf{J}$. Here c denotes concentration, D_0 is the diffusion coefficient, and $\mathbf{J} = (J_x, J_y, J_z)$ the diffusive flux. Diffusive transport can be driven by a concentration difference between an inlet and an outlet, as in the case of controlled release from pharmaceutical pellets coated with an EC/HPC polymer blend [24]. In this work, we consider a three-dimensional material with transport in the pore phase and an impermeable interface between pore and solid phase. We define the inlet to be at the bottom and outlet at the top, denoting the direction from inlet to outlet by z, and compute diffusion numerically in the z-direction. We use the steady-state diffusive flux, i.e., the solution $\mathbf{J}$ to the governing equations for which $\frac{\partial c}{\partial t} = 0$.

Diffusive transport through a pore structure can be summarized by the effective diffusion coefficient D_{eff}, defined as $\langle J_z \rangle = -D_{\text{eff}} \widetilde{\nabla} c$, where $\langle J_z \rangle$ is the average of the steady-state diffusive flux in the z-direction over the whole structure and $\widetilde{\nabla} c = (c_{\text{out}} - c_{\text{in}})/L_z$, with L_z the length of the structure in the z-direction. Here c_{in} and c_{out} are fixed concentrations at the inlet and outlet, respectively, which drive the diffusive transport. We assume that $c_{\text{in}} > c_{\text{out}}$ so the transport goes from the inlet to the outlet.

The transport ratio TR was defined in [24] as

$$TR = \frac{D_{\text{eff}}}{D_0 \epsilon}, \tag{1}$$

where ϵ denotes the pore volume fraction. By the Wiener bounds [27], we have that

$$TR \leq 1. \tag{2}$$

As discussed in [24], this bound is attained for a pore structure that has straight pores. The transport ratio measures how much slower transport is through a given pore structure than through an optimal pore structure with the same pore volume fraction.

For a pore structure with separate pores that each have constant pore size and for which the separate pores never intersect, the transport ratio satisfies

$$TR = 1/\tau^2, \tag{3}$$

where τ is the geodesic tortuosity defined below in Section 3.1.1, see [24].

Sometimes diffusive transport (or the mathematically equivalent electrical conductivity) is summarized as the resistive formation factor $F = \frac{D_{\text{eff}}}{D_0}$, or its inverse $M = 1/F$, termed the microstructure factor, relative conductivity or relative diffusivity [17,28,29]. We prefer the definition in (1), since it allows us to compare the transport efficiency between pore structures of different porosity, and relate it to an optimal pore structure. A related transport or conductivity summary is the indirect diffusional tortuosity factor, or indirect electrical tortuosity factor, which is defined as $\sqrt{1/TR}$ [28], provided e.g. by TauFactor [10]. It relates the same information as the transport ratio, but the name can easily be mis-interpreted as relating only to path-length effects when in fact it captures all effects except pore volume. It is especially easy to mis-interpret as it is often called simply tortuosity factor. Taking the square root and using the term tortuosity factor can be derived from the simple model (3), as in that case $\sqrt{1/TR} = \tau$. When we work with more complex structures, however, we prefer to use TR with its interpretation of reduction in transport compared to an optimal structure.

To aid the interpretation of diffusion flux images, we compute the relative flux $\mathbf{J}(p)/\|\mathbf{J}_{opt}\|$ as it was defined in [24], where $\mathbf{J}(p)$ is the flux computed in the point p and $\|\mathbf{J}_{opt}\| = D_0|\widetilde{\nabla}c|$ is the norm of the flux in an optimal pore structure. An optimal pore structure hence has relative flux equal to $(0,0,1)$. The transport ratio can also be computed as the average of $J_z(p)/\|\mathbf{J}_{opt}\|$, over the pore space. Thus the average is always below or equal to one even though the relative flux can take values above one in bottlenecks.

3. Pore geometry quantification methods

This section first briefly discusses existing pore geometry quantification methods, and in particular the descriptors we will use in the rest of the paper. Then our new methods for quantifying connectivity bottlenecks, the geodesic channel-strength descriptor, the pore size-channel descriptor, and the closed pore-tortuosity descriptor are described.

3.1. Existing quantification methods

3.1.1. Geodesic tortuosity

Path-length has long been considered an essential component in determining diffusive transport rates and related processes, so many definitions of tortuosity are available, see [28] for a recent review. Here we use the geodesic tortuosity, which only relies on the pore geometry for its definition.

The point-wise geodesic tortuosity $\tau(p)$, defined for a point $p \in P_{conn}$, is the length of the geodesic path $GeoPath(p)$ through the point which goes from the inlet to the outlet, divided by the distance between the inlet and the outlet of the pore structure. Here P_{conn} denotes the part of the pore space that is connected to both the top and bottom. Following [24], the *geodesic tortuosity* τ is then defined as

$$\tau = \frac{1}{|P_{conn}|} \int_{P_{conn}} \tau(p)\,dp, \tag{4}$$

i.e., the geodesic tortuosity is computed by averaging the point-wise tortuosity $\tau(p)$ over the connected pore space. This or similar geometric definitions of tortuosity have been used in e.g. [24,30–32]. Geodesic

tortuosity is sometimes computed by averaging $\tau(p)$ only over pores located at the top or bottom of the pore structure, see e.g. [14]. However, we showed in [24] that the geodesic tortuosity factor defined as in (4) by averaging over the whole pore space provides considerable improvements in explaining diffusive transport.as compared to the geodesic tortuosity defined by averaging only over the top or bottom of the pore structure.[2]

The geodesic tortuosity and the pointwise geodesic tortuosity can be computed interactively and visualized in 3D using the method `geodesic tortuosity` in MIST. This can build a basic understanding of the connectivity properties of the pore network and help to identify potential connectivity-bottlenecks.

3.1.2. 2D and 3D pore size

Pore size measurement, sometimes called granulometry, determines size of objects of complex shape using simple structuring elements and the morphological operations erosion and dilation [33–36].

The standard 3D pore size descriptor uses a spherical structuring element. For a point p in the pore space, it is defined as the size of the largest sphere that can fit in the pore space and cover p. See e.g. [37,38] for a description of how to compute the spherical pore size. Spherical pore sizes can be computed and visualized in [26] using the method `pore-size distribution` 3D.

Analogously to the spherical pore size, we can define other pore sizes by changing the structuring element. A 2D pore size, constructed using a circle oriented in one of the xy-, xz- and yz-planes, can be computed in MIST using the method `pore size distribution` 2D. We use 2D pore sizes when defining pore sizes for the Bottlenecks 1- and Bottlenecks 2-datasets in Section 4.2. This since these datasets consist of 2D pore structures with an added thickness in the third dimension.

3.1.3. Constrictivity

Constriction-bottleneck effects in a simple pore with varying pore size, such as that shown in Fig. 3(B), can be quantified using the constriction factor $A_{\min}/A_{\max}$, where $A_{\min}$ is the area of the smallest cross-section and $A_{\max}$ is the area of the largest cross-section. For more complex pore structures, a method commonly used for quantifying constrictivity uses the median of spherical pore size, $r_{\max}$, to define $A_{\max}$ and the median of the numerically simulated mercury intrusion porosimetry-pore size (MIP-pore size), $r_{\min}$, to define $A_{\min}$. MIP-pore size was defined in [37], and the constrictivity in [39]. See e.g. [9,14,24,29,39,40]; and [17] for implementations within statistical and machine learning models correlating constrictivity with diffusive transport, permeability and electrical conductivity. Alternative definitions of constrictivity have been used, see e.g. [41]; $r_{\min}$ and $r_{\max}$ have been used on their own as descriptors [17]; and so have the related descriptors the hydraulic radius [29] and the geometric constrictivity [9].

The connectivity of the pore network impacts the MIP-pore size in a point p in that there has to be a path through which a sphere of a specific size can travel to the point. Thus the connectivity also influences the constrictivity. Connectivity bottlenecks, defined as parts of the material where many paths through the path network converge, is however not captured by the constrictivity.

---

[2] In [24] we defined the geodesic tortuosity factor $\tilde{\tau}$ by $1/\tilde{\tau}^2 = \frac{1}{|P|} \int_P \frac{1}{\tau(p)^2}\, dp$. Here P denotes the full pore space and $\tau(p)$ is defined to be ∞ and $\frac{1}{\tau(p)^2}$ is defined to be zero for points p in the pore space that are not connected to the inlet and outlet. The main reason that $\tilde{\tau}$ performed better than the geodesic tortuosity defined at the top or bottom was that it is averaged over the full pore space and so uses more of the available connectivity information. As the definition of τ in (4) is simpler than the definition of the geodesic tortuosity factor $\tilde{\tau}$, and still averages over a large portion of the pore space, we prefer to use this definition of τ here.

Constrictivity and MIP-pore size in 2D and 3D are implemented in [26] through the method `intrusion porosimetry`. Constrictivity was computed from 3D MIP-pore size for the Polymer film dataset, whereas 2D versions of MIP-pore size was used for the Bottlenecks 1 and Bottlenecks 2-datasets.

3.2. Quantification of connectivity-bottlenecks

3.2.1. Geodesic channel-strength

The geodesic channel-strength [18] quantifies connectivity-bottleneck effects caused by many paths through the pore network converging in a small part of the material. It is obtained as follows: A large number of geodesic paths $G = \{GeoPath(p)\}$ corresponding to points p that are well distributed throughout the pore system are computed. Next, the pore space is divided into D boxes of equal volume. The geodesic channel-strength in each box is then obtained as the proportion of the number of paths in G that passes through the box. To summarize the channel-strength for a pore structure, we used the maximum of the channel strengths in the D boxes for the small structures considered in Section 5.1, and we used transformed quantiles and standard deviations of the channel strengths in the regression experiments in Sections 5.3 and 5.4, see Table 1.

It should be noted that an alternative computational method was used in [18]. There each path in G was given a thickness and the channel-strength in each point was computed as the number of paths passing through the point. The reason for instead dividing the space into boxes is that this is more computationally efficient.

One way of understanding connectivity in a pore structure is to find the main geodesic channels. These are obtained by combining boxes with a high channel-strength. They summarize important features of the connectivity of the pore network. Fig. 2, bottom left and right panels, illustrates how the geodesic channel-strength captures the large trends in a synthetic pore structure. There are three main channels through this structure. The middle main channel (indicated with red arrow) has strength 0.43, i.e. 43% of all geodesic paths pass through it. The geodesic channel-strength computed with two different box sizes (bottom left and bottom right panel) show roughly the same trends. The 2D-image of the pore structure was given a thickness by duplicating the image 20 times, resulting in an 3-D image with $480 \times 20 \times 270$ voxels in which diffusion was simulated numerically. The norm of the relative flux in this 3-D image (top right panel) shows that there are strong bottleneck effects, and that these correspond to the three main channels. Even though there is a high relative flux through the main channels, the overall transport ratio has a low value, $TR = 0.16$. This is because transport is inefficient in regions of the pore network that lead to the main channels, such as the pores indicated by the red rectangle in the top right panel.

The geodesic channel-strength is similar to the betweenness centrality in graph theory, which captures the relative importance of vertices in a graph [42]. However, in contrast to the betweenness centrality which is computed on graphs, the geodesic channel-strength is computed for continuous pore systems and only uses paths that connect the bottom and the top of the pore structure. This is more relevant for the application of diffusive transport driven by a concentration difference between top and bottom.

3.2.2. The pore size-channel and closed pore-tortuosity descriptors

Whether a pore is a bottleneck or not depends both on the number of paths that pass through it, i.e., on its geodesic channel-strength, and on the size of the pore and of neighbouring pores. If there is a high number of paths passing through a pore that is large then this pore is not a bottleneck for diffusive transport. Whether or not a pore with a high channel-strength is a bottleneck also depends on if there are alternative pathways that can relieve the pressure on that pore. These issues, the size of a pore with high channel-strength and the existence

of alternative pathways, are taken into account by the following two new pore geometry descriptors.

The first one, the pore size-channel descriptor, is the relative mean pore size of the channels with highest strengths, where the mean is taken of pore sizes of the voxels which have the 5% or 1% highest geodesic channel-strengths, and with the mean standardized by dividing by the mean pore size of all voxels in the pore space.

The second impact descriptor, the closed pore-tortuosity descriptor, is computed by closing pores with high channel-strength, i.e., by removing a subset of the pore space so that no paths can pass through this subset. The subsets that are closed are defined using the geodesic distance to the top as follows: The range of geodesic distance values is first divided into 100 intervals of equal length $\{I^{(1)}, \ldots, I^{(100)}\}$. Let $P^{(j)}$ be the part of the pore space with geodesic distance in interval $I^{(j)}$ and $n^{(j)}$ the number of disconnected components of the set $P^{(j)}$. Denoting such a disconnected component $P_i^{(j)}$, the pore space is partitioned into subsets $P_i^{(j)}, i = 1, \ldots, n^{(j)}, j = 1, \ldots, 100$. As we want to quantify the impact of constriction-bottlenecks, 100 of the subsets $P_i^{(j)}$ which have the 25% highest geodesic channel-strengths are chosen at random to be closed. For each such chosen subset, a modified structure is created by removing $P_i^{(j)}$ from the pore space, thus closing $P_i^{(j)}$.

The geodesic tortuosity $\tau_{modified}$ is then computed for each modified structure. We define

$$q_\tau = \begin{cases} 0 & \text{if the modified structure is disconnected,} \\ \tau_{original}/\tau_{modified} & \text{otherwise,} \end{cases}$$

where $\tau_{original}$ is the geodesic distance of the original, unmodified, structure. The closed pore-tortuosity descriptor is then set to the mean value of q_τ over the 100 modified structures for the structures in the regression experiments, and the min value of q_τ for the small structures considered in Section 5.1.

The difference in geodesic tortuosity between the original structure and a modified structure quantifies to what extent there are alternative pathways to those passing through the closed pores. An alternative way to quantify the impact of closing a pore would be to compute the geodesic channel-strength with the bottleneck closed, and compare the results with the original geodesic channel-strength. The geodesic tortuosity is however less time-consuming to compute, which is why the impact was quantified by comparing the geodesic tortuosity before and after closing pores.

4. A diffusive transport prediction experiment

This section introduces the simulation experiment which was made to study the predictive power of the different pore structure descriptors. The experiment used the polymer film and the Bottleneck 1 and 2 data sets. The reference data set was not included in the experiment.

The aim of the experiment was not just prediction, but also the understanding it gives on how different properties of pore structures influence diffusive transport. We first describe the regression models which were used for prediction, then the simulated pore structure data sets, and finally give of brief description of how diffusive transport through the structures was computed.

4.1. Multiplicative regression models

The goal is to find a model that predicts the transport ratio well from the geometry of an arbitrary pore structure. There is a long list of predictors that possibly could have a considerable effect on diffusion. Complex models that have been used include (subsets of) pore volume fraction ϵ, surface area, geodesic/geometric tortuosity τ ($mean_\tau$ and STD_τ), pore size ($mean_{PS}$, $median_{PS}$ and STD_{PS}), MIP-pore size ($mean_{MIP}$, $median_{MIP}$, and STD_{MIP}) and constrictivity descriptors as predictors [14,17,24,29,32,41]. To the best of our knowledge, connectivity-bottleneck effects have not been studied in previous work.
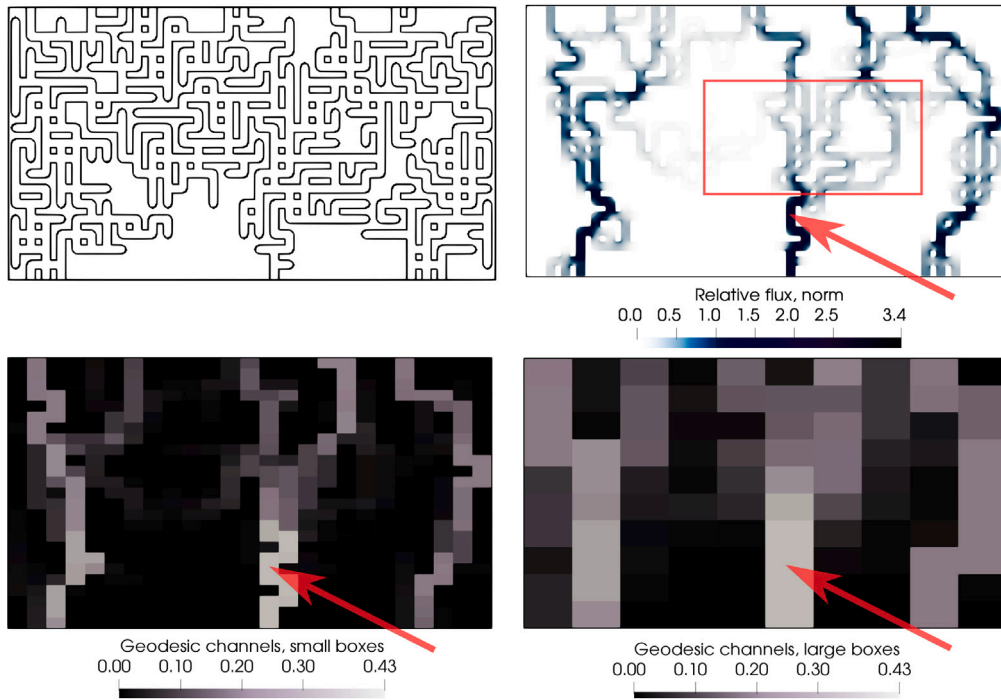
Fig. 2. 2D-illustration of geodesic channel-strength. *Top left:* the pore structure. *Top right:* diffusive transport. Relative flux > 1 indicates a bottleneck effect and relative flux < 1 indicates inefficient transport. *Bottom left:* geodesic channel-strength computed with smaller boxes. *Bottom right:* geodesic channel-strength computed with larger boxes. The red arrows in the bottom left and right panels indicate a main channel and the red arrow in the top right panel points to the corresponding bottleneck. The red rectangle indicates an area with pores which lead to the bottleneck and which have low relative flux.

Table 1
Predictors used in the multiple regression experiment.

Predictor	Explanation
τ	Geodesic tortuosity
e^{-STD_τ}	Transformed standard deviation of geodesic tortuosity
constrictivity	$median_{MIP}/median_{PS}$
$e^{-\frac{STD_{PS}}{mean_{PS}}}$	Transformed normalized standard deviation of pore sizes
$1 - 0.9 \cdot q99_{channels}$	Transformed 99% quantile of channel strength
$1 - 0.9 \cdot q95_{channels}$	Transformed 95% quantile of channel strength
$e^{-STD_{channels}}$	Transformed standard deviation of channel strength
pore size-channels	As defined in Section 3.2.2
closed pore-tortuosity	As defined in Section 3.2.2

Table 1 lists the descriptors which were used to predict diffusive transport. As discussed above we know that geodesic tortuosity is a powerful predictor of diffusive transport and has a given place in any prediction model. The descriptors $STD_{PS}/mean_{PS}$ and STD_τ were found to be relevant for diffusive transport prediction in [24]. Instead of STD_τ, we here use STD_τ/τ as a predictor in order to reduce the correlation with τ, and additionally we used the transformation e^{-x} for the predictors $STD_{PS}/mean_{PS}$ and STD_τ/τ. The $mean_{PS}$ is not a physically motivated predictor since pore size has no direct effect on diffusive transport; however, we instead used the standard deviation of the pore size divided by mean pore size as a predictor since this could be correlated with bottleneck effects caused by variations in pore size.

Three descriptors based on geodesic channel-strength were used, $1 - 0.9 \cdot q95_{channels}$, $1 - 0.9 \cdot q99_{channels}$ and $e^{-STD_{channels}}$, where $q95_{channels}$ and $q99_{channels}$ denote the 95%- and 99%-quantile of the geodesic channel-strength respectively. The transformation of the quantiles was done to obtain a positive (instead of a negative) correlation between the quantile-based predictors and TR.

To avoid overfitting, and to increase the possibility of obtaining a prediction model that could work for many types of data, we search for regression models that are sound from a physical perspective. A first step to obtain such models is to make sure that the models fits

simple pore structures for which the relationship (3) between the pore geometry and TR is known to hold. Motivated by this, we define a *core model* by the following equation,

$$TR = \frac{P}{\tau^2}, \tag{5}$$

where P is an unknown factor that take values in the interval $[0, 1]$ which can depend on different predictors. The factor P then will equal 1 pore structures for which model (3) holds. This in particular means that the core model holds for pore structures with straight pores, in which case $\tau = 1$ and the transport ratio equals 1. For more complex pore structures other factors, including bottleneck effects, influence the transport rate. The core model can be made to fit also such structures by adding these as predictors of the factor P.

We considered four different variations of (5): The first two are of the form $TR = \alpha x^{\beta_1}/\tau^\gamma$ where x is an additional predictor to be chosen and α, β_1 and γ are regression parameters to be estimated. In the first of these, we fix $\gamma = 2$, as in the core model, whereas γ is estimated for the second model. These models are termed the *one-predictor, core*-model and the *one-predictor, free exponent*-model, respectively. The next two models are the same as the first two, except that an additional predictor x_2 is added to the model, so that $TR = \alpha x_1^{\beta_1} x_2^{\beta_2}/\tau^\gamma$. These models are termed the *two-predictor, core*-model if the exponent of τ is fixed to be equal to 2 and otherwise it is called the *two-predictor, free exponent*-model. These models are displayed in Table 2. In the supplementary material models of the form $TR = \alpha x^{\beta_1}/\tau^\gamma$ with the exponent γ fixed to some value $k \in [2, k_{\max}]$ are also considered.

As in [24], we choose and estimate parameters in the models by stepwise linear regression on the logarithm of the models. Thus, the linear regression models we fit are all of the form

$$\log(y_i) = \alpha + \sum_{k=1}^{K} \beta_k \log(x_{k,i}) + \epsilon_i,$$

for $K = 1$ or 2, and where ϵ_i are independent centred Gaussian random variables, $x_{k,i}$ is the value of the k:th predictor for the i:th observation, β_k is the corresponding regression coefficient, α is an intercept, and

Table 2
Regression models. In the equations x_1 and x_2 are the predictors, α, β_1, and β_2 are parameters to be estimated.

Model name	Model equation
Core model	$TR = \dfrac{P}{\tau^2}$
One-predictor core-model	$TR = \alpha x^{\beta_1}/\tau^2$
One-predictor free exponent model	$TR = \alpha x^{\beta_1}/\tau^\gamma$
Two-predictor core-model	$TR = \alpha x_1^{\beta_1} x_2^{\beta_2}/\tau^2$
Two-predictor free exponent model	$TR = \alpha x_1^{\beta_1} x_2^{\beta_2}/\tau^\gamma$

$y = TR \cdot \tau^2$ for the core models and $y = TR$ for the free exponent-models where τ is one of the predictors. Furthermore, to obtain multiplicative regression-models that fit with the core model, the predictors were restricted to take values in the interval $[0, 1]$.

4.2. Pore structure datasets

In the regression analysis we used three data sets, the polymer film data set, the Bottlenecks 1 and the Bottlenecks 2 data sets. These are described next. We also used a reference dataset consisting of simple pore structures which should satisfy (3). The geodesic tortuosity τ of the reference pore structures varied from 1.01 to 3.42, with 222 pore structures in total.

The polymer film data set was obtained by simulation of a thresholded Gaussian random field model [43]. This model mimics the porous polymer film coatings which are used to control drug release from pharmaceutical pellets. It has parameters $\theta_{xy,\star}$ and $\theta_{z,\star}$ which control the regularity of the pore geometry in the x, y-plane and in the z-direction. A high value of $\theta_{xy,\star}$ gives pore structures that are highly regular, whereas a low value results in pore structures that have a larger variation in pore size and pore connectivity, and therefore pore structures with stronger bottleneck effects. Increasing $\theta_{z,\star}$ results in pore structures with a higher geodesic tortuosity. In this work we used four different parameter combinations $(\theta_{xy,low}, \theta_{z,low})$, $(\theta_{xy,low}, \theta_{x,high})$, $(\theta_{xy,high}, \theta_{z,low})$ and $(\theta_{xy,high}, \theta_{x,high})$ to generate pore structures. We used two different pore volume fractions for each parameter combination, creating structures differing by about 5 percentage points. The Polymer film-dataset consists of 339 pore structures in total.

The Bottlenecks 1 data set is made up of 3D-networks grown from the bottom to the top and includes 71 pore structures. The Bottlenecks 2 data set were generated from 2D-networks obtained by randomly removing edges in a regular 2D-grid and randomly assigning each edge one of two sizes. Two ratios between the smaller and larger edges were used. It consists of 280 pore structures. Details on how the datasets were produced are given in the supplementary material. The supplementary material also contains images of pore structures from each of the four datasets.

4.3. Computation

The pore geometry quantification used Matlab [44] and the geodesic distance, which is needed to compute the geodesic tortuosity and the geodesic channel-strength, was obtained using the function `bwdistgeodesic`. The sizes of the boxes used to compute the geodesic channel-strengths were different for the different datasets, and were roughly proportional to the mean pore size of the structures. The methods used to perform the geometry quantifications in this work are all included in the MIST software. The pore size-channel and close pore-tortuosity descriptors are not explicitly included in MIST, however, the pore size, geodesic tortuosity and geodesic channel-strength needed to compute them are included.

Diffusive transport was calculated numerically with the lattice-Boltzmann method in the software Gesualdo [25]. We used high precision, meaning that the tolerance stopping criterion in Gesualdo was set to a low value and that the resolution of the pore structures were high.

This meant that the computational cost was quite high, especially for the Polymer film and Bottlenecks 2 datasets, and hence a relatively low number of pore structures were simulated. All computations were performed on resources at Chalmers Centre for Computational Science and Engineering (C3SE) provided by the Swedish National Infrastructure for Computing (SNIC).

To assess the quality of the numerical computation of diffusive transport we computed mass transport through each slice in the z-direction, standardized by the mean of transport through all slices. The exact steady-state solution to the diffusion equations should have standardized mass transport through each slice equal to 1, if boundary effects are disregarded. Boundary effects were only present in the Polymer film-dataset, as the other three datasets were constructed so that the boundaries of the pore structures were solid except at the inlet and outlet. The quality of the diffusive transport computations seem to be good for all datasets, although the quality in the reference data set is somewhat lower than in the other datasets, see Figure S11 in the Supplementary Material.

5. Results

The pore structure in Fig. 2 in the introduction was taken from the Bottlenecks 2 data set. As a further illustration of the impact of bottlenecks we in the next section compare a structure with straight pores with four other somewhat more complicated pore structures cut out from this data set. Section 5.2 displays the basic features of the pore structure data sets used in the paper. The results from the multiple regression models are presented in the following sections.

5.1. Examples of impact of the new descriptors

The plots in Fig. 3 show the relative flux in five pore structures chosen to have different connectivity and constriction bottleneck effects and to make it possible to separate these from path-length effects. The corresponding values of transport ratios, geodesic tortuosities and our new descriptors are given in Table 3. The pore structures (A) - (C) all have the same geodesic tortuosity, and the differences between their transport ratios are hence caused by bottleneck effects. Structure (A) only has path-length effects. Structure (B) is the same as structure (C) except that it has constant pore size and thus only connectivity bottlenecks. Structures (C), (D), and (E) are from the Bottlenecks 2 dataset and have both connectivity and constriction bottlenecks.

Table 3 shows that the connectivity bottlenecks in (B) and (C) have a drastic effect, they make transport less than half as efficient as that in structure (A). However, in this example the added constriction bottleneck in (C) only has little impact on the transport ratio.
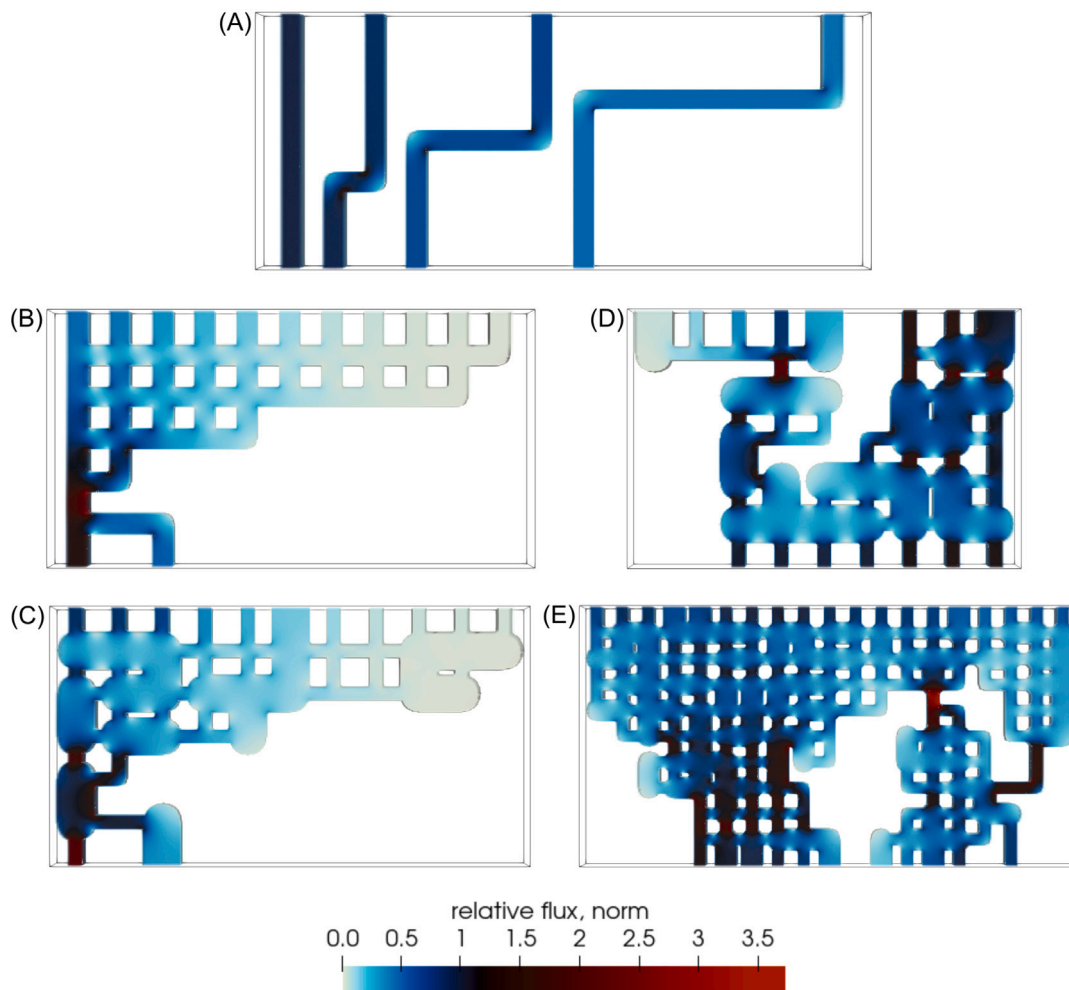
The constriction bottleneck effects are captured by the maximum channel strength. For (B) and (C) the maximum channel strengths are equal to one but for (A) the maximum strength is around four times lower, leading to the much higher transport ratio. As for structures (D) and (E), they have higher maximum channel-strengths but lower geodesic tortuosity than structure (A). These higher constriction-bottleneck effects but lower path lengths in (D) and (E) can be thought to cancel out as (A), (D) and (E) have similar transport ratios.

The pores in structures (A) and (B) have constant sizes and thus the pore size-channel descriptor is one for these structures. The pore size-channel descriptor by itself does not however discern structure (C) which has a smaller transport ratio from structures (D) and (E).

The minimum closed-pore tortuosity separates structure (A) from structures (B)-(D), but not from structure (E). Zero minimum closed-pore tortuosity here means that the structure becomes disconnected after closing a pore. It is thus clear from both the maximum channel-strength and the minimum closed pore-tortuosity that structures (B) and (C) differ from the other three in constriction bottleneck-effects.

Table 3
Transport ratios and descriptors for the pore structures in Fig. 3.

Structure	TR	Tortuosity	max channel-strength	Pore-size channel	min closed pore-tortuosity
(A)	0.59	1.32	0.23	1	0.92
(B)	0.27	1.32	1	1	0
(C)	0.26	1.32	1	0.85	0
(D)	0.55	1.08	0.42	0.89	0.84
(E)	0.57	1.07	0.36	0.86	0.94

Fig. 3. Illustration of the impact of path-length, constriction-bottlenecks and connectivity-bottlenecks on diffusive transport rates. Relative flux shown in (A) a structure with only path-length effects; (B) a structure with path-length and connectivity-bottleneck effects; and (C) - (E) structures with path-length, connectivity-bottleneck and constriction-bottleneck effects. Structures (A)–(C) have the same geodesic tortuosity. Relative flux > 1 indicates a bottleneck effect and relative flux < 1 indicates inefficient transport.

5.2. Relationship between transport ratio, geodesic tortuosity, and pore volume for the four data sets

Fig. 4 shows that the upper limit (2), $\frac{D_{eff}}{D_0} = \epsilon$, where ϵ is the pore volume, is satisfied by the polymer film, the Bottlenecks 1 and 2, and the reference data sets, as it should. The simple model (1) holds for the reference dataset and so the plot for this dataset in Fig. 5 is as expected. For the other three datasets, TR is lower than in the simple model which also is as expected as there are constrictivity and connectivity bottlenecks in these datasets. In Fig. 5 there is an approximately log-linear relationship between $1/\tau^2$ and TR when each dataset is considered separately. The results of fitting a regression model

$$\log(TR) = \alpha \log(\tau) \tag{6}$$

Table 4
Multiplicative regression-models fitted on the logarithm with no intercept.

Dataset	Fitted model	MSE
The reference-dataset	$TR = 1/\tau^{2.3}$	0.01
All datasets except the reference-dataset	$TR = 1/\tau^{5.7}$	0.05
All datasets	$TR = 1/\tau^{3.8}$	0.35

to the data sets is shown in Table 4. It can be seen that the exponents are different in the different data sets, and except for the reference data set they are far from the theoretical exponent 2.

5.3. Regression analysis of the one predictor core-model

Table 5 shows that using $1 - 0.9 \cdot q99_{channels}$ in the one predictor core-mode $TR \cdot \tau^2 = \alpha x^{\beta_1}$ (in the table called the full model) gives
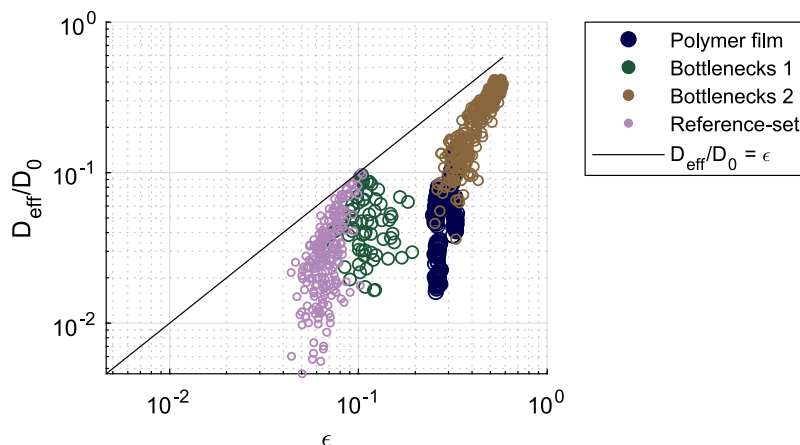
Fig. 4. $\frac{D_{eff}}{D_0}$ against pore volume ϵ on log-scale. Each circle represents one pore structure, with circles of different sizes and colours for the different data sets. The diagonal line is the bound $\frac{D_{eff}}{D_0} \le \epsilon$.
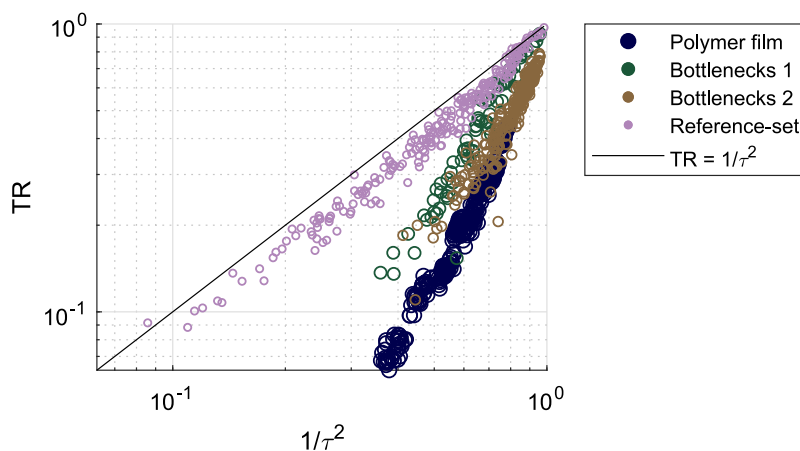

Fig. 5. TR against $1/\tau^2$ on log-scale. Each circle represents one pore structure, with circles of different sizes and colours for the different data sets. The diagonal line shows TR for the model $TR = 1/\tau^2$.

the largest reduction of MSE and of relative standard deviation of residuals, as compared to a null model $TR \cdot \tau^2 = \alpha$. The fitted models were computed from the full data sets and the values of MSE and relative standard deviations were obtained from averages of 10-fold cross-validation repeated 10 times with different partitions. Tests of the hypothesis that parameters were different from 0 gave p-values less than 0.05 for all cross-validations, except for constrictivity in all data sets, for closed pore tortuosity in the Bottlenecks 2 data set, and for $e^{-STD_{PS}/mean_{PS}}$ in the Bottlenecks 1 data set.

Table S1 in the supplementary material give the corresponding results for the one-predictor, free exponent model. It shows that if τ is included as predictor the other predictors give a much smaller reduction of MSE and of relative standard deviation. A further perspective on this is given by Table S5 in the supplementary material. It in particular shows that the one-parameter core model with $1 - 0.9 \cdot q99_{channels}$ as predictor has about the same predictive skills as the model (6).

5.4. Regression analysis of the two predictor core-model

Also for the full two predictor core-model $TR \cdot \tau^2 = \alpha x_1^{\beta_1} x_2^{\beta_2}$ the predictor $1 - 0.9 \cdot q99_{channels}$ gave the largest reduction of MSE, as compared with the null model $TR \cdot \tau^2 = \alpha$, see Table 6. The second predictor was different for the different data sets.

The fitted models were computed from the full data set and the values of MSE and relative standard deviation were obtained from the averages of 10-fold cross-validation repeated 10 times with different partitions. Tests of the hypothesis that parameters were different from 0 gave p-values less than 0.05 for all cross-validations for the three models in the table.

Table S2 in the supplementary material give the corresponding results for the two predictor, free exponent models. As for the one predictor core model, it shows that in this model the other predictors give a much smaller reduction of MSE and of relative standard deviation.

6. Discussion

Prediction using the simple model (3), i.e. the core model (5) with $P = 1$, fits the reference-dataset well, see Fig. 5 and the prediction model $TR = 1/\tau^{2.3}$ obtained in Table 4. Thus the physical theory which motivated the core model works for this data set, as it should.

Table 4 and Fig. 5 also show that the model (6), i.e. $\log(TR) = \alpha \log(\tau)$ gives relatively good predictions for the other data sets, however with rather different values of α. A reason for this could be that in these data sets there is a strong correlation between the unknown factor P in the core model and the geodesic tortuosity τ. It is expected that there should be a relatively monotone relationship between τ and the different descriptors which form part of P. It is also reasonable to expect that the relationship between P and τ would be different for different datasets. What is perhaps surprising is that the expected

Table 5
Logarithmic regression of the full one predictor core-model. The best, second best and third best MSE ratio for each dataset are in bold and the best MSE ratio is underlined. MSE ratios and relative standard deviations are not listed for models for which $\frac{MSE_{full}}{MSE_{null}} \geq 1$. The relative standard deviations for the null model where 0.19 (Polymer film), 0.23 (Bottlenecks 1) and 0.33 (Bottlenecks 2).

Predictor x	Full model $\frac{MSE_{full}}{MSE_{null}}$	$[\frac{STD_{residuals}}{mean_{response}}$, full model]
Polymer film		
Constrictivity	$TR \cdot \tau^2 = 0.3$	–, [–]
$e^{-STD_\tau/\tau}$	$TR \cdot \tau^2 = 0.5x^{5.5}$	0.85, [0.16]
Pore size-channels	$TR \cdot \tau^2 = 0.2x^{-0.8}$	0.97, [0.18]
Closed pore-tort.	$TR \cdot \tau^2 = 0.5x^{29}$	0.82, [0.15]
$e^{-STD_{PS}/mean_{PS}}$	$TR \cdot \tau^2 = 0.1x^{-6.0}$	0.84, [0.16]
$1 - 0.9 \cdot q99_{channels}$	$TR \cdot \tau^2 = 0.7x^{13}$	<u>**0.39**</u>, [0.07]
$1 - 0.9 \cdot q95_{channels}$	$TR \cdot \tau^2 = 1.1x^{46}$	**0.52**, [0.10]
$e^{-STD_{channels}}$	$TR \cdot \tau^2 = 8.5x^{0.6}$	**0.71**, [0.13]
Bottlenecks 1		
Constrictivity	$TR \cdot \tau^2 = 0.7x^{0.1}$	0.99, [0.27]
$e^{-STD_\tau/\tau}$	$TR \cdot \tau^2 = 0.7x^{1.3}$	**0.78**, [0.22]
Pore size-channels	$TR \cdot \tau^2 = 0.6$	–, [–]
Closed pore-tort.	$TR \cdot \tau^2 = 0.6x^{1.4}$	0.84, [0.23]
$e^{-STD_{PS}/mean_{PS}}$	$TR \cdot \tau^2 = 0.7x^{0.6}$	–, [–]
$1 - 0.9 \cdot q99_{channels}$	$TR \cdot \tau^2 = 0.8x^{0.9}$	<u>**0.66**</u>, [0.18]
$1 - 0.9 \cdot q95_{channels}$	$TR \cdot \tau^2 = 0.8x^{1.0}$	**0.67**, [0.18]
$e^{-STD_{channels}}$	$TR \cdot \tau^2 = 0.4x^{-0.1}$	0.89, [0.24]
Bottlenecks 2		
Constrictivity	$TR \cdot \tau^2 = 0.6$	–, [–]
$e^{-STD_\tau/\tau}$	$TR \cdot \tau^2 = 1.0x^{6.4}$	**0.68**, [0.23]
Pore size-channels	$TR \cdot \tau^2 = 0.8x^{1.0}$	0.87, [0.29]
Closed pore-tort.	$TR \cdot \tau^2 = 0.8x^{12}$	–, [–]
$e^{-STD_{PS}/mean_{PS}}$	$TR \cdot \tau^2 = 1.2x^{4.4}$	0.93, [0.31]
$1 - 0.9 \cdot q99_{channels}$	$TR \cdot \tau^2 = 1.0x^{2.0}$	<u>**0.49**</u>, [0.16]
$1 - 0.9 \cdot q95_{channels}$	$TR \cdot \tau^2 = 1.2x^{4.9}$	0.69, [0.23]
$e^{-STD_{channels}}$	$TR \cdot \tau^2 = 2.3x^{0.3}$	**0.55**, [0.18]

monotone relationship can be captured by (6), i.e., that $\log(P/\tau^2)$ can be approximated by $\alpha \log(\tau)$.

The multiplicative regression models in Sections 5.3 and 5.4 add an intercept to the model, and in some cases predictors had a negative exponent, see Tables 5 and 6. The intercept can be seen as capturing the effects in the factor P that were not included as predictors, e.g. dead-end effects. All predictors are expected to have a positive correlation with TR, and the negative exponents in some models could also indicate overfitting.

Tables S1 and S2 in the supplementary material show that for the full core models where also the geodesic tortuosity τ is used as a predictor, the other predictors contribute less to prediction in the polymer film and Bottlenecks 1 and 2 data sets. Still: (1) the physically motivated predictors, especially the $1 - 0.9 \cdot q95_{channels}$, improved prediction also when the exponent of τ was included as a parameter; (2) the high positive correlation between the connectivity-bottleneck effect caused by many paths converging in a small portion of the pore structure (geodesic channel-strength) and the path-length (geodesic tortuosity) is as expected in our data sets, which explains why the geodesic tortuosity can explain a large part of the variation on its own; and (3) the model with only geodesic tortuosity performs well when looking at each dataset separately (Fig. 5), however, when looking at all datasets together including the reference-dataset then the model fit is significantly lowered (Table 4). Thus geodesic tortuosity may explain most of the variation in a dataset when the relationship between path-lengths and other aspects of the pore structures have a simple relationship, however, more geometric descriptors are needed when including a wider range of structures. One way of taking account of a wider range of structures without expanding the dataset is to include physically motivated constraints like was done here with the one predictor- and two predictor-core models. For these constrained models we can conclude that the connectivity-bottleneck effects as measured by the geodesic channel-strength were the best predictors.

The geodesic channel-based descriptors are relatively sensitive to the size of the boxes that define channel-strength and the channel-strength in a point of the box-division is also sensitive to where the point happens to be positioned relative to the box-division. E.g. if a box divides a pore in two or if it covers a whole pore can make a clear difference for the value of the channel-strength in a point that belongs to the pore.

It is not surprising that constrictivity and $e^{-\frac{STD_{PS}}{mean_{PS}}}$ performed poorly as predictors on the two bottleneck-datasets since constriction bottlenecks were either not present (Bottlenecks 2-dataset) or likely played a less important role compared to connectivity-bottlenecks (Bottlenecks 1-dataset). That constrictivity also performed poorly on the Polymer film-dataset indicates that constriction-bottlenecks may have a relatively small influence on transport in this data set, or that the effect of constriction-bottlenecks are similar for all pore structures in the dataset.

7. Conclusions

This paper introduces three new pore structure descriptors: the geodesic channel-strength, the pore size-channel, and the closed pore-tortuosity descriptors. These three in different ways quantify connectivity-bottleneck effects caused by many paths converging in small parts of a pore structure. Connectivity-bottlenecks occur naturally in many real complex pore structures, see [18,19]. However, they are not captured by existing bottleneck-descriptors which focus on constriction-bottleneck effects caused by variations in pore size. To study the new descriptors we have constructed and analysed four data sets and developed logarithmic multiple regression models for use in prediction of diffusive transport through the structures.

Overall, geodesic tortuosity is the most important descriptor of transport. However, as described in Section 5.1, our first data set, the reference data set, provides examples which have the same tortuosities, but where diffusive transport decreases by a factor of two if there are connectivity bottlenecks in the structures. Different aspects of this were caught by our new descriptors. This data set shows that to get models which are broadly applicable and useful for many different kinds of pore structures also descriptors which capture different aspects of connectivity bottlenecks are needed. Further, the maximum relative flux in the pore structures with constrictivity-bottlenecks were more than three times as high as in the structures without bottlenecks. This can cause high strain on pores and the uneven distribution of transport (or conductivity) can potentially damage the material, see e.g. [20,21], again underlining the need for constrictivity descriptors.

The construction of the other three data sets were inspired by microscopy images of polymer films used to control drug delivery through pellet coatings. Sections 5.3 and 5.4 show that in the physically motivated core models where the exponent of tortuosity τ was set to 2 the best predictor of transport was a rescaled quantile of the geodesic channel strength. The descriptors based on the standard deviation of the geodesic channel-strength and on the standard deviation of the geodesic tortuosity also gave useful improvements of prediction. In these "polymer film" data sets the pore size-channel and the closed pore-tortuosity contributed less to prediction of transport.

To conclude, we have shown that connectivity-bottlenecks can be an important determinant for diffusive transport rate by reducing transport efficiency and that they can put a high strain on the pores in the bottlenecks. Care needs to be taken when modelling the relationship between pore geometry and diffusive transport, as path-lengths can be strongly correlated with connectivity-bottleneck effects.

The geodesic tortuosity, the geodesic channel-strength, the constrictivity, and the 2D- and 3D-pore size descriptors which used in this paper can all be computed using the software [26]. For poorly connected pore structures with potential connectivity-bottlenecks, we recommend to first explore connectivity interactively in 3D using the geodesic

Table 6
Logarithmic regression of the full two predictor core-model. Column 2 of the table shows the number out of the 36 two-predictor models that had lower MSE than the best one-predictor model. The best full model had $x_1 = 1 - 0.9 \cdot q99_{channels}$ for all three datasets. x_2 is listed in the table.

	# better models	Best full model		
		Full model;		$\frac{MSE_{full}}{MSE_{null}}$, $\left[\frac{STD_{residuals}}{mean_{response}}\right]$
Polymer film	6	$x_2 = e^{-\frac{STD_{PS}}{mean_{PS}}}$,	$TR \cdot \tau^2 = 0.4 x_1^{13} x_2^{-1.9}$;	0.35 [0.08]
Bottlenecks 1	5	$x_2 = e^{-STD_{channels}}$,	$TR \cdot \tau^2 = 0.5 x_1^{0.4} x_2^{-0.1}$;	0.59 [0.16]
Bottlenecks 2	5	$x_2 = e^{-STD_\tau/\tau}$,	$TR \cdot \tau^2 = 1.1 x_1^{1.2} x_2^{3.0}$;	0.38 [0.12]

tortuosity as can be done in MIST, and then to use geodesic channel-strength to quantify any connectivity-bottlenecks. Further information can, if needed, be obtained from the pore size-channels and closed pore-tortuosity.

CRediT authorship contribution statement

Sandra Barman: Writing – review & editing, Writing – original draft, Software, Methodology, Formal analysis, Conceptualization. **Holger Rootzén:** Writing – review & editing, Supervision, Methodology, Funding acquisition, Conceptualization. **David Bolin:** Writing – review & editing, Supervision, Methodology, Conceptualization.

Data statement

Code and data required to recreate the results, shown in figures in the paper, are provided in the Supplementary.

Declaration of competing interest

The authors declare that they have no known competing financial interests or personal relationships that could have appeared to influence the work reported in this paper.

Acknowledgements

Appendix A. Supplementary data

Supplementary material related to this article can be found online at https://doi.org/10.1016/j.commatsci.2025.113942.

Data availability

Data and code needed to recreate results are provided in the Supplementary.

References

[1] D. Heng, P. Tang, J. Cairney, H. Chan, D. Cutler, R. Salama, J. Yun, Focused-ion-beam milling: a novel approach to probing the interior of particles used for inhalation aerosols, Pharm. Res. 24 (9) (2007) 1608–1617.

[2] J. James, H.-W. Choi, J. Pharoah, X-ray computed tomography reconstruction and analysis of polymer electrolyte membrane fuel cell porous transport layers, Int. J. Hydrog. Energy 37 (23) (2012) 18216–18230.

[3] L. Anovitz, D. Cole, Characterization and analysis of porosity and pore structures, Rev. Miner. Geochem. 80 (1) (2015) 61–164.

[4] A. Jones, C. Arns, D. Hutmacher, B. Mithorpe, A. Sheppard, M. Knackstedt, The correlation of pore morphology, interconnectivity and physical properties of 3D ceramimc scaffolds with bone ingrowth, Biomaterials 30 (7) (2009) 1440–1451.

[5] J. Siepmann, R. Siegel, M. Rathbone (Eds.), Fundamentals and Applications of Controlled Drug Delivery, Springer, New York, 2012.

[6] D. Markl, A. Strobel, R. Schlossnikl, J. Bøtker, P. Bawuah, C. Ridgway, J. Rantanen, T. Rades, P. Gane, K.-E. Peiponen, J. Zeitler, Characterization of pore structures of pharmaceutical tablets: a review, Int. J. Pharm. 538 (2018) 188–214.

[7] M. Wang, P. Ning, Predictions of effective physical properties of complex multiphase materials, Mater. Sci. Eng.: R: Rep. 63 (1) (2008) 1–30.

[8] A. Weber, R. Borup, R. Darling, P. Das, T. Dursch, W. Gu, D. Harvey, A. Kusoglu, S. Litster, M. Mench, R. Mukundan, J. Owejan, J. Pharoah, M. Secanell, I. Zenyuka, A critical review of modeling transport phenomena in polymer-electrolyte fuel cells, J. Electrochem. Soc. 161 (2) (2014) F1254–F1299.

[9] F. Usseglio-Viretta, D. Finegan, A. Colclasure, T. Heenan, D. Abraham, P. Shearing, K. Smith, Quantitative relationships between pore tortuosity, pore topology, and solid particle morphology using a novel discrete particle size algorithm, J. Electrochem. Soc. 167 (10) (2020) 100513.

[10] S. Cooper, A. Bertei, P. Shearing, J. Kilner, N. Brandon, TauFactor: An open-source application for calculating tortuosity factors from tomographic data, SoftwareX (2016).

[11] J. Owen, The resistivity of a fluid-filled porous body, J. Pet. Technol. 4 (7) (1952) 169–174.

[12] E. Petersen, Diffusion in a pore of varying cross section, AIChE J. 5 (1958) 343–345.

[13] R.A. Siegel, Porous systems, in: J. Siepmann, R.A. Siegel, M.J. Rathbone (Eds.), Fundamentals and Applications of Controlled Release Drug Delivery, Springer, New York, 2012, pp. 229–251.

[14] O. Stenzel, O. Pecho, L. Holzer, M. Neumann, V. Schmidt, Predicting effective conductivities based on geometric microstructure characteristics, AIChE J. 62 (2016) 1834–1843.

[15] C. Berg, Permeability description by characteristic length, tortuosity, constriction and porosity, Transp. Porous Media 103 (3) (2014) 381–400.

[16] O. Pecho, O. Stenzel, B. Iwanschitz, P. Gasser, M. Neumann, V. Schmidt, M. Prestat, T. Hocker, R. Flatt, L. Holzer, 3D microstructure effects in Ni-YSZ anodes: prediction of effective transport properties and optimization of redox stability, Materials 8 (9) (2015) 5554–5585.

[17] B. Prifling, M. Röding, P. Townsend, M. Neumann, V. Schmidt, Large-scale statistical learning for mass transport prediction in porous materials using 90,000 artificially generated microstructures, Front. Mater. 8 (786502) (2021) http://dx.doi.org/10.3389/fmats.2021.786502.

[18] S. Barman, C. Fager, M. Röding, N. Lorén, C. von Corswant, E. Olsson, D. Bolin, H. Rootzén, New characterization measures of pore shape and connectivity applied to coatings used for controlled drug release, J. Pharm. Sci. 110 (7) (2021) 2753–2764, http://dx.doi.org/10.1016/j.xphs.2021.02.024.

[19] C. Fager, S. Barman, M. Röding, N. Lorén, C. von Corswant, D. Bolin, H. Rootzén, E. Olsson, 3D high spatial resolution visualisation and quantification of interconnectivity in polymer coatings, Int. J. Pharm. 587 (119622) (2020) http://dx.doi.org/10.1016/j.ijpharm.2020.119622.

[20] S. Harris, P. Lu, Effects of inhomogeneities–nanoscale to mesoscale–on the durability of Li-Ion batteries, J. Phys. Chem. C 117 (3) (2013) 6481–6492.

[21] S. Müller, J. Eller, M. Ebner, C. Burns, J. Dahn, V. Wood, Quantifying inhomogeneity of lithium ion battery electrodes and its influence on electrochemical performance, J. Electrochem. Soc. 165 (2) (2018) A339.

[22] S. Alizadeh, M. Bazant, A. Mani, Impact of network heterogeneity on electrokinetic transport in porous media, J. Colloid Interface Sci. 553 (2019) 451–464.

[23] F. Henrique, P. Żuk, A. Gupta, A network model to predict ionic transport in porous materials, Proc. Natl. Acad. Sci. USA 121 (22) (2024) e2401656121.

[24] S. Barman, H. Rootzén, D. Bolin, Prediction of diffusive transport through polymer films from characteristics of the pore geometry, AIChE J. 65 (1) (2019) 446–457.

[25] T. Gebäck, A. Heintz, A lattice Boltzmann method for the advection-diffusion equation with Neumann boundary conditions, Commun. Comput. Phys. 15 (2) (2014) 487–505.

[26] MIST, A Program Package for Visualization and Characterization of 3D Geometries, 2019, URL https://mist.math.chalmers.se,

[27] O. Wiener, Die theorie des mischkörpers für das feld der stationären strömung, Abh. der Math.- Phys. Kl. der Königl. Sächsischen Ges. der Wiss. 32 (1912) 509–604.

[28] L. Holzer, P. Marmet, M. Fingerle, A. Wiegmann, M. Neumann, V. Schmidt, Tortuosity and Microstructure Effects in Porous Media: Classical Theories, Empirical Data and Modern Methods, Springer, Switzerland, 2023, http://dx.doi.org/10.1088/1361-6501/ac354a.

[29] M. Neumann, O. Stenzel, F. Willot, L. Holzer, V. Schmidt, Quantifying the influence of microstructure on effective conductivity and permeability: Virtual materials testing, Int. J. Solids Struct. (2020) 211–220, http://dx.doi.org/10.1016/j.ijsolstr.2019.03.028.

[30] R. Brémond, D. Jeulin, P. Gateau, J. Jarrin, G. Serpe, Estimation of the transport properties of polymer composites by geodesic propagation, J. Microsc. 176 (2) (1994) 167–177.

[31] C. Peyrega, D. Jeulin, Estimation of tortuosity and reconstruction of geodesic paths in 3D, Image Anal. Stereol. 32 (1) (2013) 27–43.

[32] M. Röding, Z. Ma, S. Torquato, Predicting permeability via statistical learning on higher-order microstructural information, Sci. Rep. 10 (2020) 15239, http://dx.doi.org/10.1038/s41598-020-72085-5.

[33] G. Matheron, Eléments Pour Une Théorie Des Milieux Poreux, Masson, Paris, 1967.

[34] P. Delfiner, A generalization of the concept of size, J. Microsc. 95 (2) (1972) 203–216.

[35] J. Serra, Image Analysis and Mathematical Morphology, Academic Press, Inc., Orlando, 1982.

[36] P. Soille, Morphological Image Analysis: Principles and Applications, second ed., Springer Berlin Heidelberg, 2004.

[37] B. Münch, L. Holzer, Contradicting geometrical concepts in pore size analysis attained with electron microscopy and mercury intrusion, J. Am. Ceram. Soc. 91 (12) (2008) 4059–4067.

[38] J. Ohser, K. Schladitz, 3D Images of Materials Structures: Processing and Analysis, John Wiley & Sons, 2009.

[39] L. Holzer, D. Weidenmann, B. Münch, L. Keller, M. Prestat, P. Gasser, I. Robertson, B. Grobéty, The influence of constrictivity on the effective transport properties of porous layers in electrolysis and fuel cells, J. Mater. Sci. 48 (7) (2013) 2934–2952.

[40] L. Holzer, B. Iwanschitz, T. Hocker, L. Keller, O. Pecho, G. Sartoris, P. Gasser, B. Muench, Redox cycling of Ni–YSZ anodes for solid oxide fuel cells: Influence of tortuosity, constriction and percolation factors on the effective transport properties, J. Power Sources 242 (2013) 179–194.

[41] C. Berg, Re-examining archie's law: Conductance description by tortuosity and constriction, Phys. Rev. E: Stat. Nonlinear, Soft Matter Phys. 86 (4) (2012) 046314.

[42] M. Newman, Networks, second ed., Oxford University Press, Oxford, 2018.

[43] S. Barman, D. Bolin, A statistical model for imaged microstructures of porous polymer films, J. Microsc. 269 (3) (2019) 247–258.

[44] MATLAB, Version R2022a, The MathWorks Inc., Natick, Massachusetts, 2022.